Received: 17 May 2023 | Revised: 1 August 2023 | Accepted: 15 August 2023

IET Generation, Transmission & Distribution

DOI: 10.1049/gtd2.12972

The Institution of Engineering and Technology WILEY

ORIGINAL RESEARCH

# A novel travelling-wave direction criterion for hybrid multi-terminal HVDC system

Botong Li[1] | Yuqi Li[1] | Bin Li[1] | Xiaolong Chen[1] | Liang Ji[2] | Qiteng Hong[3]

[1]Department of Electrical Engineering, Tianjin University, Tianjin, China

[2]Department of Electrical Power Engineering, Shanghai University of Electric Power, Shanghai, China

[3]Department of Electronic and Electrical Engineering, University of Strathclyde, Glasgow, UK

**Correspondence**
Botong Li, Department of Electrical Engineering, Tianjin University, Tianjin, China.
Email: libotong@tju.edu.cn

**Funding information**
Joint Funds of the National Natural Science Foundation of China, Grant/Award Number: U2166205

**Abstract**

Fast and accurate fault direction criteria are crucial for efficient protection in hybrid multi-terminal HVDC transmission systems. The current variation method is commonly used to identify fault direction, but it is affected by fault resistance and distributed capacitance. This paper proposes a new direction criterion based on the backward fault travelling wave, which has stronger resistance to interference from transition resistance and operates at a faster speed than other methods. Additionally, this paper provides the time-domain expression of the travelling wave after multiple reflections between the fault point and the converter station port, enabling the calculation of the threshold setting for the criterion. The new direction criterion is tested in PSCAD/EMTDC, and simulation results demonstrate that it can accurately identify fault direction and has a strong ability to withstand transition resistance.

## 1 | INTRODUCTION

The hybrid multi-terminal HVDC system (MTDC) has evolved from the dual-terminal HVDC system, inheriting the advantages of high reliability, economical efficiency, and flexible transmission [1, 2]. In contrast to other HVDC systems, the hybrid MTDC system is particularly well suited for multi-power supply and multi-receiver power transmission, making it a promising choice with broader application prospects [3, 4].

In the hybrid MTDC system, the converter station at the sending end generally adopts the line commutation converter (LCC) to achieve better economic efficiency, while the converter station at the receiving end adopts the modular multi-level converter (MMC) to avoid commutation failure [5, 6]. Due to the presence of the MMC converter station, in the event of a DC overhead line (OHL) fault occurring in the hybrid MTDC system, the current rises rapidly. Thus, it becomes imperative to promptly and accurately identify and disconnect the faulted OHL to ensure the safe operation and rapid recovery of the non-fault section of the system [7, 8]. To achieve quicker response times, the main protection of the hybrid MTDC system generally employs non-unit protection [9]. Given that the two OHLs are directly connected at the intermediate converter station of the system, the main protection at this position must be equipped with a direction unit to differentiate between forward and backward faults, ensuring the selectivity of the action [10]. In the hybrid MTDC system, a rapid and accurate direction criterion plays a critical role in identifying faulted transmission lines.

The identification of fault direction through current variation is a widely used method. However, the accuracy of this method is influenced by factors such as fault resistance [11, 12]. Travelling-wave (TW) reflection and refraction occur when the fault TW sent by the fault point spreads to the line ends. The reflection and refraction characteristics of TW can be utilized as the characteristic quantity for direction identification. The direction criterion exhibits strong robustness to high-resistance faults [13]. Another study [14] identifies the fault direction by comparing the ratio of the high-frequency components of the forward and backward TWs. However, both the TW direction criteria proposed in [13, 14] are based on the differences of TW

characteristics obtained from simulations, and the setting values also rely on simulations.

In order to address the limitations of TW protection criteria, which lack theoretical support and depend on simulations for setting values, several scholars have investigated the analytic expression method of TW in HVDC systems. They have applied this method to design new TW protection schemes and calculate the setting values of the criteria [15]. In [16], the analytic expression of voltage TW at different line boundaries of a hybrid three-terminal HVDC system is derived, leading to the proposal of a fast protection scheme for dc lines based on the time of the first extreme value of fault voltage. Reference [17] analyzes TW characteristics at the bus bar in a hybrid three-terminal HVDC system, deriving the complex frequency domain expression of the fault initial TW, and utilizing it for setting values in TW protection. But [16, 17] mainly focus on the analytical calculation of the first TW; they do not consider the influence of secondary or multiple TWs. Particularly, when the fault point is near the end of the line, the time interval between the first TW and subsequent TWs becomes very short, making it indistinguishable. In such cases, analyzing only the first TW for fault characteristics may lead to malfunctions in relevant protection schemes. Hence, it is imperative to conduct research on the fault characteristics of TW after multiple reflections and refractions in a short time under the condition of near and remote end OHL faults. This is necessary to ensure that the fault direction criterion can function accurately.

In this paper, the analytic calculation method of fault voltage TW at the protection of the intermediate converter station is studied. The time-domain expressions of TW after multiple reflections and refractions in a short time under the near and remote end fault of the OHL are derived emphatically. According to the analysis of the differences in TW characteristics between forward and backward faults, a novel direction criterion based on the amplitude characteristics of the backward TW is proposed, and the theoretical calculation method of setting value is given. A simulation model of the Kun-Liu-Long hybrid three-terminal HVDC system is also built to verify the reliability and robustness of the direction criterion.

## 2 | ANALYSIS OF TW FAULT CHARACTERISTICS

This paper takes the Kun-Liu-Long hybrid three-terminal HVDC system as the research reference. The basic topology of the system is depicted in Figure 1. LCC converter station is used at the sending end of the system, and MMC is adopted at both converter stations at the receiving end.

The LCC station connects the $MMC_1$ station with the OHL L1. The $MMC_1$ station connects the $MMC_2$ station with the OHL L2, and the OHL L1 and L2 are connected to the $MMC_1$ station through the confluent bus. Table 1 shows the detailed system parameters [14].

MMC, modular multi-level converter; OHL, overhead line.

In a bipolar dc transmission system, electromagnetic coupling exists between OHLs after the line fault occurs. For the purpose of simplifying the analysis, the phase-mode transformation is applied to achieve electromagnetic decoupling. The phase-mode transformation equation is shown as

$$\begin{bmatrix} i_0 \\ i_1 \end{bmatrix} = \frac{1}{2}\begin{bmatrix} 1 & 1 \\ 1 & -1 \end{bmatrix}\begin{bmatrix} i_p \\ i_n \end{bmatrix} \quad \begin{bmatrix} u_0 \\ u_1 \end{bmatrix} = \frac{1}{2}\begin{bmatrix} 1 & 1 \\ 1 & -1 \end{bmatrix}\begin{bmatrix} u_p \\ u_n \end{bmatrix} \tag{1}$$

where $i$ and $u$ represent current and voltage, and the zero-mode and line-mode components are denoted by the subscripts 0 and 1, respectively.

There exist line-mode components after faults occur for both pole-to-pole(P-P) and pole-to-ground(P-G) faults, and the attenuation and distortion of the line-mode components on OHLs are relatively small. Therefore, this study employs line-mode components for the identification of the direction criterion. Within 1 ms after the fault occurs, the system control link does not play a significant role, so the influence of control link can be ignored, and the system can be approximately regarded as a linear system. In order not to be affected by the load component, according to the superposition theorem of the linear system, this paper only analyzes the faulty component.

The direction criterion of the measuring point m at the confluent bus of the $MMC_1$ converter station is studied in this paper. When the fault occurs on OHL L2, it is considered a forward fault, and when the fault occurs on OHL L1, it is considered a backward fault, as shown in Figure 2. The fault location diagram is also shown in Figure 2, where $f_1$ is located at any position on the OHL L1, $f_2$ is located near the head of the OHL L2, $f_3$ is located at the non-port position of the OHL

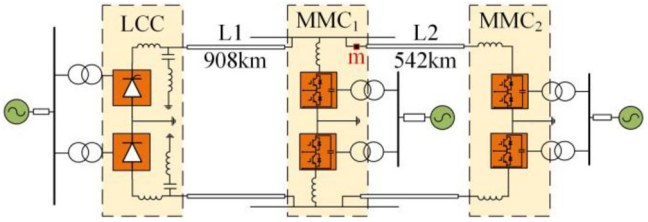


**FIGURE 1** The topology of the Kun-Liu-Long hybrid three-terminal DC system.

**TABLE 1** Parameters of system.

| Parameters | Value |
|---|---|
| Length of L1, L2 (km) | 908,542 |
| Rated DC voltage (kV) | 800 |
| Rated AC voltage (kV) | 525 |
| Outlet inductance of MMC (H) | 0.075 |
| Bridge arm inductance of MMC (H) | 0.1 |
| Submodule capacitance of MMC (F) | 0.015 |
| Line-mode impedance of OHL (Ω) | 232 |
| Zero-mode impedance of OHL (Ω) | 581 |
| Attenuation coefficient of the OHL | $6 \times 10^{-5}$ |

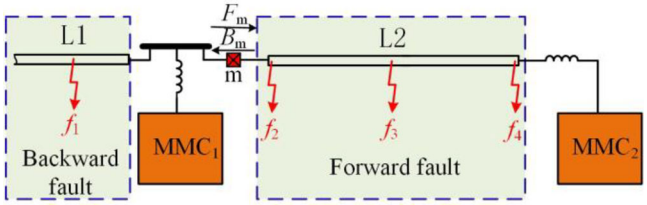


**FIGURE 2** The schematic diagram of the fault location.

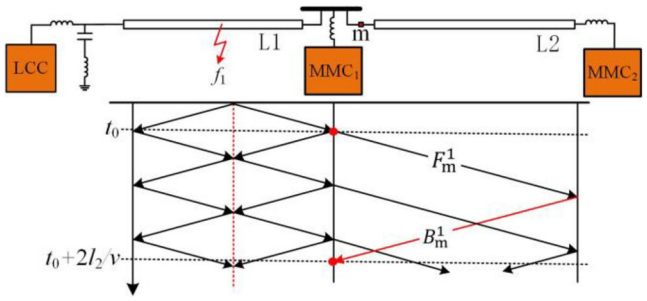


**FIGURE 3** The schematic diagram of fault TW transmission after $f_1$ fault. TW, travelling wave.

L2, $f_4$ is located near the end of the OHL L2, and m is at the head of OHL L2. This section illustrates the backward fault TW (BFTW) characteristics of the point m after the fault happens on different positions of the OHL L1 and L2.

## 2.1 | BFTW characteristics at m in case of the OHL L1 fault

After a fault occurs at $f_1$ on OHL L1, the fault TW transmission process is shown in Figure 3. According to Figure 3, the forward fault TW sent from the point $f_1$ refracts after reaching the measuring point m to form the forward TW $F_m^1$ on OHL L2 at time $t_0$. $F_m^1$ reflects at the end of OHL L2, then reaches m again forming the BFTW $B_m^1$.

It can be seen that before the TW $B_m^1$ reaches the point m, the BFTW cannot be detected at m, so the expression of the TW $B_m$ is shown as (2). $v$ is the propagation velocity of line-mode TW, and $l_2$ is the length of OHL L2. (2) is valid for faults occurring at any position of OHL L1.

$$B_m = 0 (t_0 \le t \le t_0 + \frac{2l_2}{v}) \tag{2}$$

## 2.2 | BFTW characteristics at m in case of the OHL L2 fault

This section analyzes the characteristics of TWs at the protection measurement point m after faults occur at various locations on line L2. Specifically, the faults occurring near the head of the OHL, those occurring away from the near end, and those occurring near the end of the OHL are studied separately.

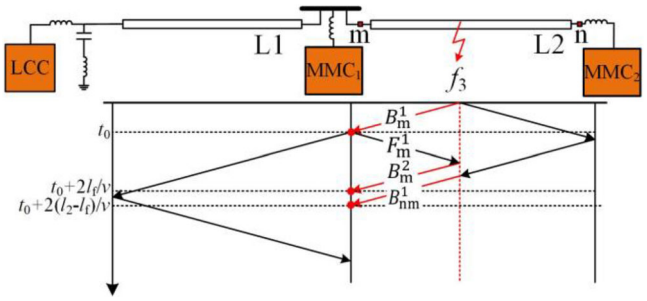


**FIGURE 4** The schematic diagram of fault TW transmission after $f_3$ fault. TW, travelling wave.

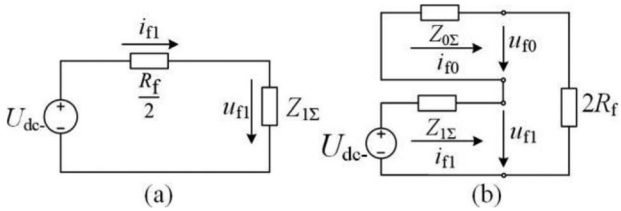


**FIGURE 5** The equivalent fault additional mode network (a) P-P fault, (b) P-G fault. P-G, pole-to-ground; P-P, pole-to-pole.

### 2.2.1 | 2.2.1 BFTW characteristics at m in case of fault at point $f_3$

The fault point $f_3$ is located at the non-end position, neither near the head nor near the end of the OHL L2. When the fault occurs at $f_3$, the fault TW transmission process is shown in Figure 4.

According to [18], the equivalent fault additional mode network at fault point $f_3$ can be obtained respectively after the P-G fault and the P-P fault occur on the line L2, as is shown in Figure 5. In the figure, $U_{dc-}$ is the negative voltage of the line L2 under the condition of system normal operation. $R_f$ is the transition resistance, and $Z_{1\Sigma}$ and $Z_{0\Sigma}$ are the equivalent line-mode and ground-mode impedances at the fault point. $i_{f1}$ and $i_{f0}$ are the line-mode and ground-mode current flowing into the fault point. $u_{f0}$ and $u_{f1}$ are the zero-mode and line-mode voltages at the fault point. $Z_{c1}$ and $Z_{c0}$ are the line-mode and zero-mode wave impedances of the OHL L2, respectively.

According to Figure 5, the expression of the BFTW $B_f^1$ at the fault point after the P-P fault and P-G fault occur on the OHL L2 can be calculated and shown as

$$B_f^1 = \begin{cases} \dfrac{2U_{dc-}Z_{c1}}{R_f + Z_{c1}} & \text{P} - \text{Pfault} \\ \dfrac{2U_{dc-}Z_{c1}}{Z_{c1} + Z_{c1} + 4R_f} & \text{P} - \text{Gfault} \end{cases} \tag{3}$$

At time $t_0$, the TW $B_m^1$ reaches m at the head of the OHL L2, $B_m^1$ reflects at m, and forms the forward TW $F_m^1$. $F_m^1$ arrives at the fault point $f_3$ again, and reflects at $f_3$ then the TW $B_m^2$ is formed. At the same time, the forward TW sent from the

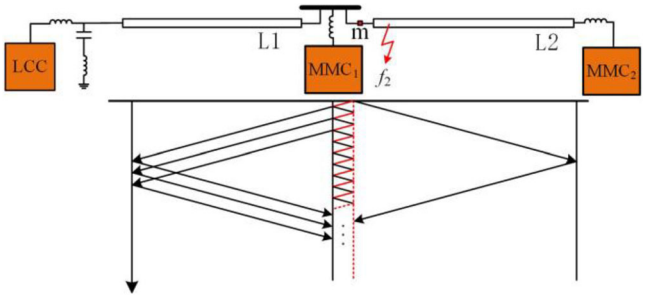


**FIGURE 6** The schematic diagram of fault TW transmission after $f_2$ fault. TW, travelling wave.

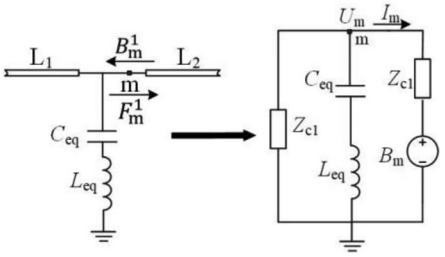


**FIGURE 7** The equivalent circuit diagram at the point m.

fault point reflects at n, then refracts at the fault point, and forms the TW $B^1_{nm}$. Analyzing the TW transmission process, there is only the TW $B^1_m$ at m before the TW $B^2_m$ and $B^1_{nm}$ reach m.

The BFTW $B^1_f$ at $f_3$ is transmitted to m at the head of the OHL L2 and the BFTW $B^1_m$ is formed. During the process, the TW $B^1_f$ will be attenuated. According to the above analysis, there is only the first TW $B^1_m$ at the point m before the TW $B^2_m$ and $B^1_{nm}$ reach the point m. The expression of the TW $B_m$ can be expressed as (4). $l_f$ is the distance between $f_3$ and m, $l_2$ is the length of the line L2 and $k_a$ is the attenuation coefficient of the OHL.

$$B_m = \begin{cases} \dfrac{2(1-k_a l_f)U_{dc}-Z_{c1}}{R_f + Z_{c1}} & P-Pfault \\ \dfrac{2(1-k_a l_f)U_{dc}-Z_{c1}}{Z_{c1}+Z_{c1}+4R_f} & P-Gfault \end{cases} \quad (t_0 \le t \le \min\{t_0 + 2\frac{l_f}{v}, t_0 + 2\frac{(l_2-l_f)}{v}\}) \tag{4}$$

According to (4), if $l_f$ is close to 0 or $l_2$, that is, the fault point is near the head or end of the OHL L2, the time frame of (4) will become very small. However, it is necessary to analyze the data in the determined time window $T_w$ in the actual fault line identification, so that the value range of fault distance $l_f$ established by Equation (4) can be obtained, as shown in (5).

$$\frac{vT_w}{2} \le l_f \le l_2 - \frac{vT_w}{2} \tag{5}$$

If the fault distance $l_f$ does not meet the conditions shown in (5), that is, the fault point is considered to be near the head or the end of the OHL L2, these two conditions can be regarded as near and remote faults. Equation (4) is not valid and further discussions are needed separately.

### 2.2.2 | 2.2.2 BFTW characteristics at m in case of fault at $f_2$

The fault point $f_2$ is located near the head of the OHL L2. The fault TW transmission process is shown in Figure 6. The BFTW sent from $f_2$ will soon reach the measurement point m. Since $f_2$ is close to m, the BFTW will be reflected multiple times between $f_2$ and m in the time window $T_s$.

Therefore, for the near end fault, when analyzing the BFTW $B_m$ at m, the influence of the superposition of TWs after multiple reflections should be taken into account.

The expression of the first TW $B^1_m$ at m can be obtained according to (4). $B^1_m$ reflects at the confluent bus to form a forward TW $F^1_m$. The equivalent circuit during the TW reflection is shown in Figure 7 [19]. In the figure, $C_{eq}$ is the equivalent capacitance of the MMC station, $L_{eq}$ is the sum of the equivalent inductance of the MMC station and the inductance of the current limiting reactor at the outlet of the MMC station.

On the basis of the equivalent circuit, the voltage $U_m$ and current $I_m$ at m in the complex frequency domain satisfy the relationship shown in (6).

$$\begin{cases} \left[\dfrac{U_m(s)}{Z_{c1}} + I_m(s)\right] \cdot \left(sL_{eq} + \dfrac{1}{sL_{eq}}\right) = U_m(s) \\ U_m(s) - Z_{c1}(s) \cdot I_m(s) = B^1_m(s) \end{cases} \tag{6}$$

The BFTW $B^1_m$ reflects at m and the forward TW $F^1_m$is formed. $F^1_m$ can be expressed as

$$F^1_m(s) = U_m(s) + Z_{c1}(s) \cdot I_m(s) \tag{7}$$

Combining (6) with (7), the expression of the forward TW $F^1_m$ can be deduced as

$$F^1_m(s) = \frac{Z_{c1} \cdot B^1_m(s)}{2sL_{eq} + \frac{2}{sC_{eq}} - Z_{c1}} \tag{8}$$

The forward TW $F^1_m$ reflects at the fault point $f_2$ again and the BFTW $B^2_m$ is formed. Different fault types have different reflect conditions at the fault point. The expression of BFTW $B^2_m$ can be obtained, which can be expressed as

$$B^2_m(s) = \begin{cases} \dfrac{Z_{c1}}{Z_{c1}+R_f} \cdot F^1_m(s) & P-Pfault \\ \dfrac{Z_{c0}+4R_f}{Z_{c1}+Z_{c0}+4R_f} \cdot F^1_m(s) & P-Gfault \end{cases} \tag{9}$$

The backward TW $B_m^2$ reaches the point m again and reflects, and thus forms the forward TW $F_m^2$. According to (6) and (7), the expression of $F_m^2$ can be obtained as

$$F_m^2(s) = \frac{Z_{c1} \cdot B_m^2(s)}{2sL_{eq} + \frac{2}{sC_{eq}} - Z_{c1}} \tag{10}$$

Based on the above analysis and combined with (8) and (9), the expression of backward TW $B_m^i$ after the $i$th reflection can be expressed as follows:

$$B_m^i(s) = \begin{cases} \left(\frac{Z_{c1}}{Z_{c1}+R_f}\right)^{i-1} \cdot \\ \left(\frac{sZ_{c1}C_{eq}}{2s^2C_{eq}L_{eq} - sC_{eq}Z_{c1} + 2}\right)^{i-1} \cdot B_m^1(s) \quad \text{P} - \text{Pfault} \\ \left(\frac{Z_{c0}+4R_f}{Z_{c1}+Z_{c0}+4R_f}\right)^{i-1} \cdot \\ \left(\frac{sZ_{c1}C_{eq}}{2s^2C_{eq}L_{eq} - sC_{eq}Z_{c1} + 2}\right)^{i-1} \cdot B_m^1(s) \quad \text{P} - \text{Gfault} \end{cases} \tag{11}$$

The expression of backward TW $B_m^i(s)$ after each reflection in complex frequency domain is transformed to time domain using the *Inverse Laplace Transform*, then the time-domain characteristics of TW $B_m^i$ are analyzed. In the following analysis, the P-P fault is used as an illustration, and the condition of P-G fault is similar.

Based on (4), the first backward TW $B_m^1$ in time domain can be obtained as follows:

$$B_m^1(t) = \frac{2U_{dc-}Z_{c1}}{R_f + Z_{c1}} \tag{12}$$

The second backward TW $B_m^2(s)$ is converted into time-domain expression. According to Table 1, $Z_{c1}^2/16L_{eq}^2$ is much larger than $1/C_{eq}L_{eq}$, and $B_m^2(s)$ can be simplified as follows:

$$B_m^2(s) = \frac{U_{dc-}Z_{c1}^3}{L_{eq}(Z_{c1}+R_f)^2} \cdot \frac{1}{s\left(s - \frac{Z_{c1}}{2L_{eq}}\right)} \tag{13}$$

The time-domain expression of (13) can be obtained by the *Inverse Laplace Transform*

$$B_m^2(t) = \frac{2U_{dc-}Z_{c1}^2}{(Z_{c1}+R_f)^2}\left(e^{\frac{Z_{c1}}{2L_{eq}}t} - 1\right) \tag{14}$$

Similarly, the expression $B_m^3(t)$ can be obtained as

$$B_m^3(t) = \frac{2U_{dc-}Z_{c1}^3}{(Z_{c1}+R_f)^3}\left(\frac{Z_{c1}}{2L_{eq}}te^{\frac{Z_{c1}}{2L_{eq}}t} - e^{\frac{Z_{c1}}{2L_{eq}}t} + 1\right) \tag{15}$$

Substituting the parameters in Table 1 into $B_m^2(t)$ and $B_m^3(t)$, when $t$ is less than 0.2 ms, it can be calculated that $B_m^2$ is much larger than $B_m^3$. Therefore, it is considered that $B_m^3$ can be ignored. It should be noted that although the specific parameters may differ in actual projects, the order of magnitude remains the same. The quantitative relationship between $B_m^2$ and $B_m^3$ differs by more than two orders of magnitude; therefore, $B_m^3$ can be ignored even the parameters change. Moreover, $B_m^n$ can be ignored when n is bigger than 2 and $t$ is less than 0.2 ms, which can be proved as follows:

For the n+1*th* backward TW $B_m^{n+1}(s)$ simplification

$$B_m^{n+1}(s) = \frac{2Z_{c1}^{2n+1}U_{dc-}}{(2L_{eq})^n(Z_{c1}+R_f)^n} \cdot \frac{1}{s\left(s - \frac{Z_{c1}}{2L_{eq}}\right)^n} \tag{16}$$

Carry out the *Inverse Laplace Transform* on (16); it can be obtained

$$B_m^{n+1}(t) = \frac{2Z_{c1}^{2n+1}U_{dc-}}{(2L_{eq})^n(Z_{c1}+R_f)^n}\int_0^t \frac{t^n}{n!} \cdot e^{\frac{Z_{c1}}{2L_{eq}}t}\,dt \tag{17}$$

According to (17), it can be calculated that

$$B_m^{n+1}(t) + \frac{Z_{c1}}{Z_{c1}+R_f} \cdot B_m^n(t) = \frac{2Z_{c1}^{2n}U_{dc-}}{(2L_{eq})^{n-1}(Z_{c1}+R_f)^n n!} \cdot t^n e^{\frac{Z_{c1}}{2L_{eq}}t} \tag{18}$$

According to (18), the following inequality can be obtained:

$$\frac{2Z_{c1}^{2n}U_{dc-}}{(2L_{eq})^{n-1}(Z_{c1}+R_f)^n n!} \cdot t^n e^{\frac{Z_{c1}}{2L_{eq}}t} < B_m^{n+1}(t) + B_m^n(t) < \frac{2Z_{c1}^{2n-1}U_{dc-}}{(2L_{eq})^{n-1}(Z_{c1}+R_f)^{n-1} n!} \cdot t^n e^{\frac{Z_{c1}}{2L_{eq}}t} \tag{19}$$

According to (19), it can be obtained that

$$B_m^{n+1}(t) < B_m^{n-1}(t) \tag{20}$$

According to (20), when n is greater than two, $B_m^2$ is much larger than $B_m^n$, so $B_m^n$ can be ignored when $t$ is less than 0.2 ms. The expression of $B_m$ is shown in Equation (21), where $t_0$ is the time when the backward TW $B_m^2$ reaches m. When $t$ is greater

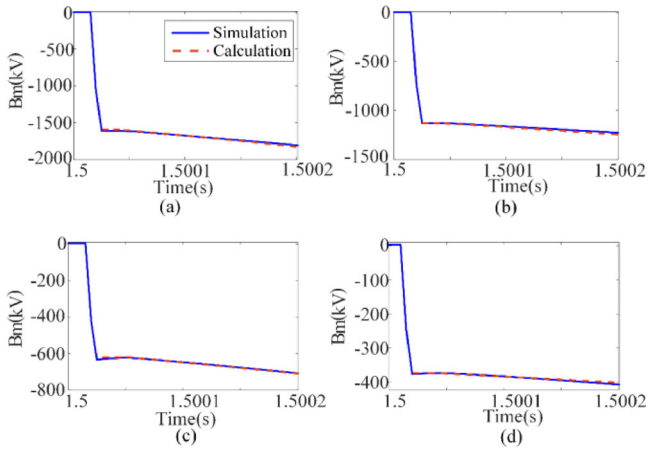


**FIGURE 8** Comparison between $B_m$ simulation waveform and analytical waveform in case of $f_2$ fault (a) P-P fault with 0 Ω, (b) P-P fault with 100 Ω, (c) P-G fault with 0 Ω, (d) P-G fault with 100 Ω. P-G, pole-to-ground; P-P, pole-to-pole.

than zero, $\varepsilon(t)$ is one; otherwise $\varepsilon(t)$ is zero.

$$B_m = \sum_{i=1}^{n} B_m^i = B_m^1 + B_m^2 = \begin{cases} \frac{2U_{dc}-Z_{c1}}{R_f+Z_{c1}} + \frac{2U_{dc}-Z_{c1}^2}{(Z_{c1}+R_f)^2} \cdot \\ \left[ e^{\frac{Z_{c1}}{2L_{eq}}(t-t_0)} - 1 \right] \varepsilon(t-t_0) & \text{P-P fault} \\ \frac{2U_{dc}-Z_{c1}}{Z_{c1}+\ Z_{c0}+4R_f} + \frac{2U_{dc}-Z_{c1}Z_{c0}}{(Z_{c1}+Z_{c0}+4R_f)^2} \cdot \\ \left[ e^{\frac{Z_{c1}}{2L_{eq}}(t-t_0)} - 1 \right] \varepsilon(t-t_0) & \text{P-G fault} \end{cases} \quad (21)$$

To ensure that the theoretical analysis conclusion is correct, P-G fault and P-P fault are set at $f_2$, which is 5 km away from the head of the OHL L2. The fault resistance is 0 and 100 Ω, respectively, and the time when the fault occurs is set to 1.5 s. Simulation and analytical waveforms of the BFTW $B_m$ at m within 0.2 ms after the fault can be obtained, as shown in Figure 8.

From Figure 8, it can be found that the analytical waveform is basically consistent with the simulation waveform, which verifies the expression of $B_m$.

### 2.2.3 | 2.2.3 BFTW characteristics at m in case of fault at $f_4$

The point n is at the end of the OHL L2, and the fault point $f_4$ is located near n. After fault occurs, the fault TW transmission process is shown in Figure 9. Because $f_4$ is close to n, the fault TW sent from $f_4$ will have multiple reflections between $f_4$ and n

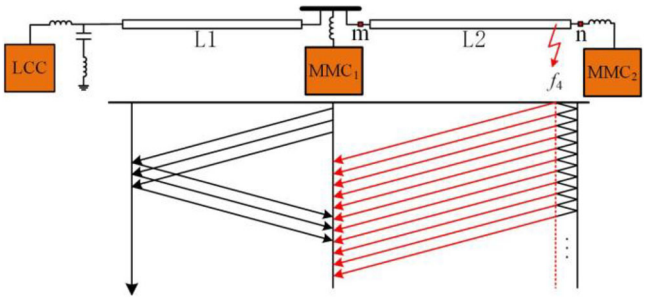


**FIGURE 9** The schematic diagram of fault TW transmission after $f_4$ fault. TW, travelling wave.

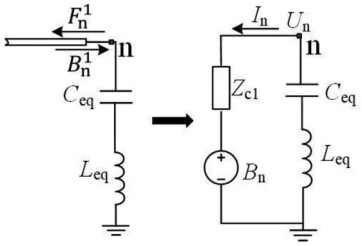


**FIGURE 10** The equivalent circuit diagram at the end of line L2.

in a short period. Therefore, as for the remote fault at the line L2, when analyzing the TW $B_m$ at m, the superposition result of the first backward TW from $f_4$ to m and the multiple refraction TWs should be considered.

The equivalent circuit diagram at n after TW reflection can be derived, as shown in Figure 10.

Because $f_4$ is close to n, the influence of the OHL on the attenuation and distortion of the TW $B_f^1$ can be ignored, that is, $B_f^1$ and $B_n^1$ are approximately the same. The backward TW $B_f^1$ at fault point can be solved according to (4). Then, combined with the equivalent circuit at n, it can be expressed as

$$\begin{cases} U_n(s) = -I_n(s) \cdot (sL_{eq} + \frac{1}{sC_{eq}}) \\ U_n(s) - Z_{c1}(s) \cdot I_n(s) = B_n^1(s) \end{cases} \quad (22)$$

The backward TW $B_n^1$ reflects at n and forms a forward TW $F_n^1$. For $F_n^1$

$$F_n^1(s) = U_n(s) + Z_{c1}(s) \cdot I_n(s) \quad (23)$$

According to (22) and (23), the expression of forward TW $F_n^1$ at n is described as

$$F_n^1(s) = \frac{(s - \frac{Z_{c1}}{L_{eq}}) \cdot B_n^1(s)}{s + \frac{Z_{c1}}{L_{eq}}} \quad (24)$$

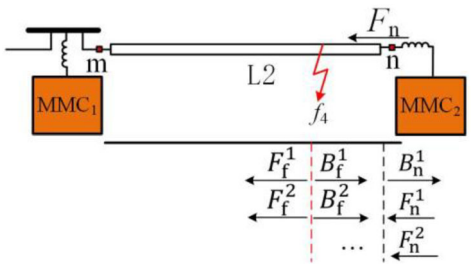


**FIGURE 11** The schematic diagram of fault TW reflection and refraction. TW, travelling wave.

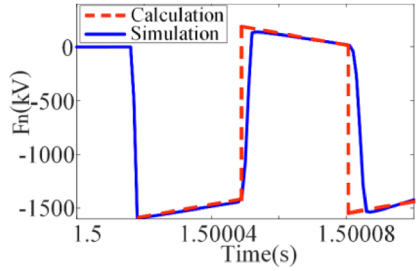


**FIGURE 12** The simulation and analytical waveform of the forward TW $F_n$ at n. TW, travelling wave.

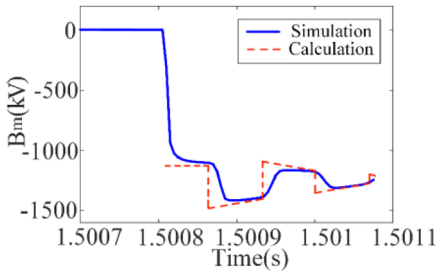


**FIGURE 13** The simulation and analytical waveform of the TW $B_m$ in case of the OHL L2 remote fault. OHL, overhead line; TW, travelling wave.

The TW $F_n^1$ soon reaches the fault point $f_4$ again, and reflection will occur at the fault point to form a backward TW $B_f^2$, and meanwhile refraction occurs to form the forward TW $F_f^2$. The forward TW $F_f^2$ will propagate to m at the head of the OHL L2, and the backward TW $B_f^2$ will reach n again and reflect; thus, the forward TW $F_n^2$ is formed. Figure 11 shows the TW transmission process.

According to (9) and (24), the forward TW $F_n^i$ at n after the $i$th reflection of the line L2 fault can be obtained that

$$F_n^i(s) = \begin{cases} \left(\frac{Z_{c1}}{Z_{c1}+R_f}\right)^{i-1} \cdot \left(\frac{sL_{eq}-Z_{c1}}{sL_{eq}+Z_{c1}}\right)^{i} \cdot B_n^1(s) & \text{P}-\text{Pfault} \\ \left(\frac{Z_{c0}+4R_f}{Z_{c1}+Z_{c0}+4R_f}\right)^{i-1} \cdot \left(\frac{sL_{eq}-Z_{c1}}{sL_{eq}+Z_{c1}}\right)^{i} \cdot B_n^1(s) & \text{P}-\text{Gfault} \end{cases} \tag{25}$$

Equation (25) is first simplified to analyze the time-domain characteristics of the forward TW $F_n^i$ after $i$th reflection. Taking the P-P fault at $f_4$ of the OHL L2 as an example, the P-G fault is similar. On the basis of (25), $F_n^i$ can be simplified as

$$F_n^i(s) = \left(\frac{Z_{c1}}{Z_{c1}+R_f}\right)^{i-1} \cdot \left(1 - \frac{2\frac{Z_{c1}}{L_{eq}}}{s+\frac{Z_{c1}}{L_{eq}}}\right)^{i} \cdot \frac{2U_{dc-}Z_{c1}}{R_f+Z_{c1}} \cdot \frac{1}{s} \tag{26}$$

By binomial expansion of $F_n^i(s)$, it can be described as

$$F_n^i(s) = (-1)^i \cdot \left(\frac{Z_{c1}}{Z_{c1}+R_f}\right)^{i-1} \cdot \frac{2U_{dc-}Z_{c1}}{R_f+Z_{c1}} \cdot \frac{1}{s} + 2 \cdot (-1)^{i+1} \cdot \left(\frac{Z_{c1}}{Z_{c1}+R_f}\right)^{i-1} \cdot \frac{2U_{dc-}Z_{c1}}{R_f+Z_{c1}} \cdot \frac{1}{s+\frac{Z_{c1}}{L_{eq}}} + o\left(\frac{1}{\left(s+\frac{Z_{c1}}{L_{eq}}\right)^2}\right) \tag{27}$$

In (27), $o$ represents a higher-order term. If the higher-order term is transformed by the *Inverse Laplace Transform*, the transformed time-domain expression contains the product term of time $t$, which is almost zero in the $T_w$ time period selected in this paper, so it can be ignored in the analysis. The time-domain expression of the forward TW $F_n^i$ can be obtained by applying the *Inverse Laplace Transform* to (28), and thus it can be obtained that

$$F_n^i(t) = (-1)^i \cdot \left(\frac{Z_{c1}}{Z_{c1}+R_f}\right)^{i-1} \cdot \frac{2U_{dc-}Z_{c1}}{R_f+Z_{c1}} + 2 \cdot (-1)^{i+1} \cdot \left(\frac{Z_{c1}}{Z_{c1}+R_f}\right)^{i-1} \cdot \frac{2U_{dc-}Z_{c1}}{R_f+Z_{c1}} \cdot e^{-\frac{Z_{c1}}{L_{eq}}t} \tag{28}$$

According to (28), when a metallic fault occurs, for each TW arrival time, and $t = 0$, it is described as

$$F_n^i(0) = 2 \cdot (-1)^{i+1} U_{dc-} \tag{29}$$

According to (29), after each backward TW is reflected at point n to form a forward TW, the amplitude of the forward TW should be the opposite of the previous amplitude, namely, a sudden change occurs. According to (28) and (29), it can be analyzed that the TW after each reflection has a tendency of changing suddenly at first and then it changes gradually. The forward TW $F_n$ expression is shown in (30). $\Delta t_f$ is the time interval of the two adjacent forward TWs after reflection.

$$F_n(t) = \sum_{i=1}^{k} F_n^i[t-(i-1)\Delta t_f]\varepsilon(t-(i-1)\Delta t_f) \tag{30}$$

When a metallic P-P fault occurs at 5 km away from n at 1.5 s, the TW $F_n$ simulation waveform under this fault condition

can be obtained, and the analytic waveform can be illustrated according to (28) and (30), as shown in Figure 12.

According to (28) and (30), the extreme value of TW $F_n$ in the time window $T_s$ after fault can be calculated, as shown in (31).

$$\min(F_n) = \begin{cases} \dfrac{2U_{dc-}Z_{c1}}{R_f + Z_{c1}} & P-Pfault \\ \dfrac{2U_{dc-}Z_{c1}}{Z_{c1} + Z_{c0} + 4R_f} & P-Gfault \end{cases}$$

$$\max(F_n) = \begin{cases} \dfrac{2U_{dc-}Z_{c1}R_f}{(R_f + Z_{c1})^2} - \dfrac{2U_{dc-}Z_{c1}}{R_f + Z_{c1}} \cdot 2e^{-\frac{Z_{c1}}{L_{eq}}T_w} & P-Pfault \\ \dfrac{2U_{dc-}Z_{c1}^2}{(Z_{c1} + Z_{c0} + 4R_f)^2} - \dfrac{2U_{dc-}Z_{c1}}{Z_{c1} + Z_{c0} + 4R_f} \cdot 2e^{-\frac{Z_{c1}}{L_{eq}}T_w} & P-Gfault \end{cases} \quad (31)$$

The forward TW $F_n$ at n first propagates to $f_4$, and then refracts at $f_4$ to form the TW $F_{nf}$, which continues to spread to m at the head of the OHL L2. According to the TW refraction formula, $F_{nf}$ can be expressed as

$$F_{nf} = \begin{cases} \dfrac{R_f}{R_f + Z_{c1}} \cdot F_n & P-Pfault \\ \dfrac{Z_{c1}}{Z_{c1} + Z_{c0} + 4R_f} \cdot F_n & P-Gfault \end{cases} \quad (32)$$

The TW $B_m$ received at m is composed of two parts, the backward TW $B_f$ directly generated from $f_4$ and the forward TW $F_{nf}$ reflected at the end of OHL L2 and then refracted by $f_4$. Ignoring the attenuation and distortion effects of the OHL on the TW, the TW $B_m$ can be expressed as

$$B_m = B_f + F_{nf} \quad (33)$$

To ensure that the theoretical analysis conclusion is correct, P-G fault with a resistance of 100 Ω is set at $f_4$, which is 5 km away from the end of the OHL L2. The TW $B_m$ simulation waveform and analytical waveform at m can be obtained, as shown in Figure 13. According to Figure 13, the simulation waveform is basically consistent with the analytical waveform in the variation trend and value range.

## 3 | FAULT DIRECTION CRITERION

The starting time at protection m after line fault is set as $t_0$, and the criterion of protection starting unit is

$$\left|\frac{dU_m}{dt}\right| > \Delta_1 \quad (34)$$

In (34), $U_m$ denotes the voltage at point m, and $\Delta_1$ is the setting threshold. During the setting process, the abrupt change of voltage rate caused by voltage fluctuation during normal system operation should be avoided.

According to the four fault conditions analyzed in Section 2, the value range of TW $B_m$ in the time window $T_s$ can be obtained.

When the fault occurs on the OHL L1, $B_m$ is 0 before the reflected TW reaches m.

When the fault occurs at $f_2$, according to (21), the value range of $B_m$ within $T_s$ can be obtained as follows:

$$\frac{2U_{dc-}Z_{c1}}{R_f + Z_{c1}} + \frac{2U_{dc-}Z_{c1}^2}{(Z_{c1} + R_f)^2}\left(e^{\frac{Z_{c1}}{2L_{eq}}T_w} - 1\right) \le B_m \le \frac{2U_{dc-}Z_{c1}}{Z_{c1} + Z_{c0} + 4R_f} \quad (35)$$

When the fault occurs at $f_3$, according to (4), the value range of $B_m$ can be obtained as follows:

$$\frac{2(1 - k_a l_f)U_{dc-}Z_{c1}}{R_f + Z_{c1}} \le B_m \le \frac{2(1 - k_a l_f)U_{dc-}Z_{c1}}{Z_{c1} + Z_{c0} + 4R_f} \quad (36)$$

When the fault occurs at $f_4$, according to (3), (31)–(33) the value range of $B_m$ within $T_s$ can be calculated as follows:

$$\frac{2U_{dc-}(1 - k_a l_f)(Z_{c1} + 2R_f)Z_{c1}}{(R_f + Z_{c1})^2} \le B_m \le \frac{2U_{dc-}(1 - k_a l_f)Z_{c1}}{Z_{c1} + Z_{c0} + 4R_f}\left[1 + \frac{Z_{c1}}{Z_{c1} + Z_{c0} + 4R_f} \cdot 2e^{-\frac{Z_{c1}}{L_{eq}}T_w} + \frac{Z_{c1}^2}{(Z_{c1} + Z_{c0} + 4R_f)^2}\right] \quad (37)$$

From the above analysis, in the time period of $t_0 < t < t_0 + T_w$, if the fault occurs on the OHL L1, the TW $B_m$ is 0. While, if the fault occurs on line L2, it can be seen from (35), (36), and (37) that $B_m$ is negative and has a maximum value. The maximum value is obtained, as shown in (38).

$$\max(B_m) = \frac{2U_{dc-}(1 - k_a l_f)Z_{c1}}{Z_{c1} + Z_{c0} + 4R_f}\left[1 + \frac{Z_{c1}}{Z_{c1} + Z_{c0} + 4R_f} \cdot 2e^{-\frac{Z_{c1}}{L_{eq}}T_w} + \frac{Z_{c1}^2}{(Z_{c1} + Z_{c0} + 4R_f)^2}\right]$$

For the measuring point m, the fault on the OHL L1 is regarded as a backward fault, while the fault on the OHL L2 is regarded as a forward fault. In order to identify the fault direction, the threshold $K_{set}$ can be set. If

$B_m$ is less than $K_{set}$, it is determined as a forward fault; otherwise, it is a backward fault. $K_{set}$ can be set as the maximum value of the backward TW $B_m$ after the OHL L2 (forward) fault. $B_m$ is always negative after the OHL L2 (forward) fault. To improve the sensitivity of the fault direction identification, the threshold $K_{set}$ can be demonstrated as follows:

$$K_{set} = 0.2\max(B_m) = \frac{0.4U_{dc-}(1-k_a l_f)Z_{c1}}{Z_{c1}+Z_{c0}+4R_f} \left[1 + \frac{Z_{c1}}{Z_{c1}+Z_{c0}+4R_f} \cdot 2e^{-\frac{Z_{c1}}{L_{eq}}T_w} + \frac{Z_{c1}^2}{(Z_{c1}+Z_{c0}+4R_f)^2}\right] \tag{39}$$

The fault direction criterion is shown as (40), where $\Delta i_{m1}(k)$ and $\Delta u_{m1}(k)$ are the fault components of line-mode current and voltage at m.

$$\begin{cases} \Delta u_{m1}(k) - Z_{c1}\Delta i_{m1}(k) \geq K_{set} & \text{backwardfault} \\ \text{Otherwise} & \text{forwardfault} \end{cases} \tag{40}$$

According to the fault analysis in Section 2.2, the time window $T_w$ is set as 0.2 ms. Criterion (40) is to detect whether the BFTW $B_m$ exceeds the threshold $K_{set}$ within 0.2 ms after the fault start-up unit trips.

According to (38), after a forward fault, max($B_m$) is negative. The derivative of max ($B_m$) expression shows that it increases with the rise of transition resistance. Therefore, in the $K_{set}$ setting calculation, the transition resistance $R_f$ is set as 500 Ω to ensure the accuracy of identification under high resistance fault conditions.

## 4 | SIMULATION VERIFICATION

Taking the Kun-Liu-Long hybrid three-terminal HVDC system as the referent, the simulation model is established in PSCAD/EMTDC. Table 1 displays the specific system parameters. The fault point $f_1$ is located at the midpoint of the OHL L1, the fault points $f_2$, $f_3$, and $f_4$ are respectively located 10 km from the head of the OHL L2, in the middle of the OHL L2 and 10 km from the end of the OHL L2. The fault location can be seen in Figure 2. The transmission line mode is frequency-dependent and the tower model is shown as Figure 14.

According to the fault analysis in Section 2.2, the time window $T_w$ is set as 0.2 ms and the threshold $K_{set}$ can be calculated as −22.3 kV by bringing the parameters in Table 1 into (39). The threshold $\Delta_1$ of fault start-up unit is set as 25 kV/ms. The fault time is set as 1.5 s and the sampling frequency of the protection device is 50 kHz.

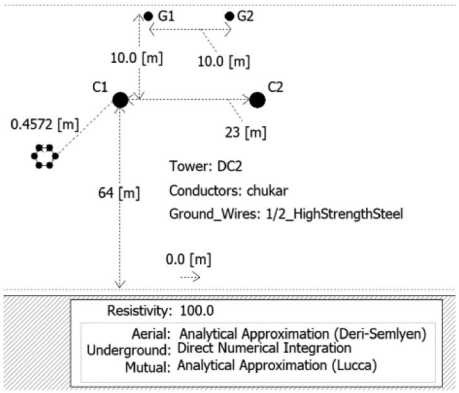


**FIGURE 14** The tower model of the OHL. OHL, overhead line.

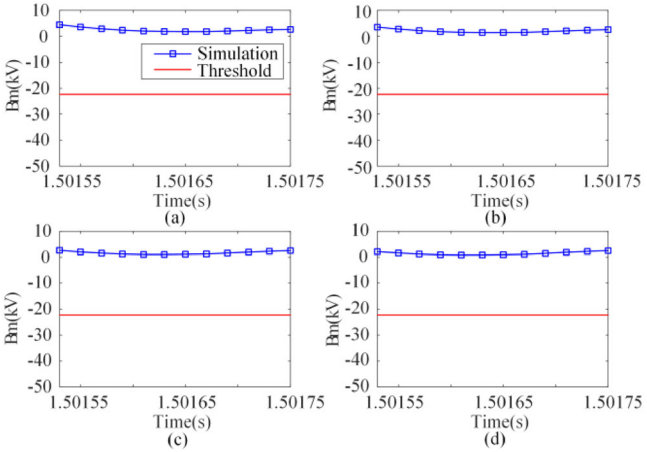


**FIGURE 15** The simulation waveform and threshold curve in case of $f_1$ fault: (a) P-P fault with 0 Ω, (b) P-P fault with 100 Ω, (c) P-G fault with 0 Ω, (d) P-G fault with 100 Ω. P-G, pole-to-ground; P-P, pole-to-pole.

### 4.1 | BFTW characteristics at m in case of the OHL L2 fault.

When a fault occurs at $f_1$ on the OHL L1, the simulation waveform and threshold curve of backward TW $B_m$ at m are shown in Figure 15. The fault types are P-P fault and P-G fault. The time shown by the red dotted line in the figure is the start time of the protection, and the time window is 0.2 ms.

Figure 15 demonstrates that the TW $B_m$ after the OHL L1 fault is approximately 0 and is greater than the threshold $K_{set}$ within the time window. Therefore, it can be accurately obtained that the faults occur on the OHL L1, and determine it as a forward fault.

### 4.2 | Verification of judgment in case of the OHL L2 fault

When a fault occurs on the OHL L2, the simulation waveform and threshold curve of the backward TW $B_m$ at m after the fault

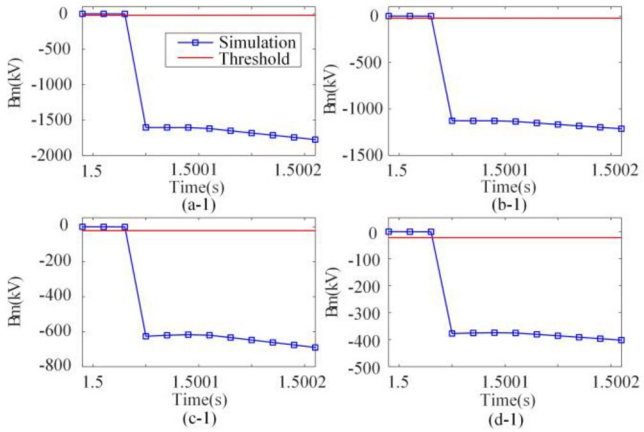


**FIGURE 16** The simulation waveform and threshold curve in case of $f_2$ fault: (a) P-P fault with 0 Ω, (b) P-P fault with 100 Ω, (c) P-G fault with 0 Ω, (d) P-G fault with 100 Ω. P-G, pole-to-ground; P-P, pole-to-pole.

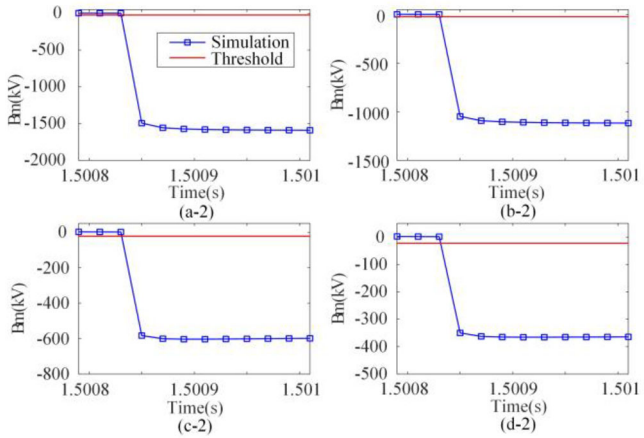


**FIGURE 17** The simulation waveform and threshold curve in case of $f_3$ fault: (a) P-P fault with 0 Ω, (b) P-P fault with 100 Ω, (c) P-G fault with 0 Ω, (d) P-G fault with 100 Ω. P-G, pole-to-ground; P-P, pole-to-pole.

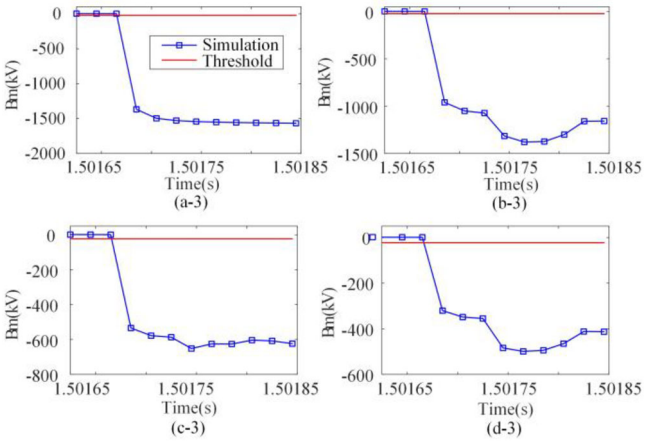


**FIGURE 18** The simulation waveform and threshold curve in case of $f_4$ fault: (a) P-P fault with 0 Ω, (b) P-P fault with 100 Ω, (c) P-G fault with 0 Ω, (d) P-G fault with 100 Ω. P-G, pole-to-ground; P-P, pole-to-pole.

**TABLE 2** Robustness test of high-resistance fault.

| Fault type | Fault point | Max($B_m$) (kV) | Min($B_m$) (kV) | Fault direction |
|---|---|---|---|---|
| P-G fault | $f_1$ | 7.3 | −1.2 | Backward |
| | $f_2$ | −146 | −213 | Forward |
| | $f_3$ | −141 | −159 | Forward |
| | $f_4$ | −199 | −249 | Forward |
| P-P fault | $f_1$ | 6.9 | −1.4 | Backward |
| | $f_2$ | −515 | −697 | Forward |
| | $f_3$ | −505 | −536 | Forward |
| | $f_4$ | −672 | −815 | Forward |

at $f_2$, $f_3$, and $f_4$ on the OHL L2 can be obtained, as shown in Figures 16 to 18 separately.

It can be seen from Figures 16–18 that the TW $B_m$ after the OHL L2 fault is always negative and significantly less than $K_{set}$ within the time window. Therefore, this method can accurately identify the fault occurs on OHL L2 and determine it as a forward fault.

## 4.3 | Robustness test of high-resistance fault

In order to test the robustness to high-resistance fault of the criterion proposed in this paper, the transition resistance is set as 500 Ω. The minimum value of TW $B_m$ in case of backward fault and the maximum value of TW $B_m$ in case of forward fault are obtained, as shown in Table 2.

According to Table 2, in the case of high-resistance fault, min($B_m$) after backward fault is higher than $K_{set}$. After the forward fault, max($B_m$) is less than $K_{set}$. It is demonstrated that the method proposed in this paper is still applicable in the case of a P-G fault with a transition resistance of 500 Ω and has a strong robustness to high-transition resistance.

## 4.4 | Robustness test of noise

Gaussian white noise with a signal-to-noise ratio of 20 dB is superimposed on the TW $B_m$ to evaluate the anti-noise capability of the criteria established in this paper. As shown in Table 3, the minimum value of the TW $B_m$ in case of the backward fault and the maximum value of the TW $B_m$ in case of the forward fault is obtained.

According to Table 3, min($B_m$) is much larger than $K_{set}$ in the case of backward fault, and max($B_m$) is much smaller than $K_{set}$ in the case of forward fault, which proves that the criterion is still applicable under the condition of noise interference has a strong robustness to noise interference.

**TABLE 3** Robustness test of noise.

| Fault type | Fault point | Max($B_m$) (kV) | Min($B_m$) (kV) | Fault direction |
|---|---|---|---|---|
| P-G fault | $f_1$ | 5.3 | −1.5 | Backward |
| | $f_2$ | −245 | −323 | Forward |
| | $f_3$ | −255 | −271 | Forward |
| | $f_4$ | −337 | −436 | Forward |
| P-P fault | $f_1$ | 7.4 | −1.2 | Backward |
| | $f_2$ | −772 | −893 | Forward |
| | $f_3$ | −749 | −761 | Forward |
| | $f_4$ | −887 | −973 | Forward |

**TABLE 4** Comparison between Siemens criterion.

| Fault resistance(Ω) | Fault point | $\Delta i$ (kA) | Fault direction | Max ($B_m$) (kV) | Fault direction |
|---|---|---|---|---|---|
| 100 | $f_2$ | 1.67 | Forward | −403 | Forward |
| | $f_3$ | 0.85 | Forward | −378 | Forward |
| | $f_4$ | 0.69 | Forward | −369 | Forward |
| 500 | $f_2$ | 0.62 | Forward | −146 | Forward |
| | $f_3$ | 0.31 | / | −141 | Forward |
| | $f_4$ | 0.23 | / | −199 | Forward |

### 4.5 | Comparison with other direction criterion

Reference [20] employs the current variation $\Delta i$ as the characteristic quantity for the direction criterion. The fault direction criterion can be expressed as

$$\Delta i > \Delta_1 \text{(Forward fault)} \tag{41}$$

To avoid the influence of current fluctuations under the normal system operation and load power change, the threshold $\Delta_1$ is selected as 0.35 kA. The direction criterion in [20] and the criterion proposed in this paper are respectively tested, and the fault type is P-G fault. Table 4 displays the test result.

According to Table 4, the direction criterion proposed by [20] can identify the fault direction when the fault resistance is 100 Ω. But the judgment fails when the fault resistance is 500 Ω, while the criterion proposed in this study can still correctly judge.

## 5 | CONCLUSION

The analytical calculation method of voltage TW after the fault occurs at OHL in the hybrid three-terminal HVDC system is studied and a direction criterion based on the characteristics of the backward TW is proposed in this paper. The contributions and innovations of this paper are as follows:

1. For the first time, the time-domain expression of the backward TW after multiple reflections and refractions is derived when the fault occurs at the near and remote end of the OHL, and the difference of the TW between the forward fault and the backward fault is revealed.
2. A new direction criterion based on the amplitude of the backward TW is proposed, which realizes accurate and quick direction identification and does not rely on the line boundary element. The setting value is directly calculated through system parameters instead of depending on the simulation.

## AUTHOR CONTRIBUTION

Botong Li, (Conceptualization, Methodology); Yuqi Li, (Data curation, editing); Bin Li, (Reviewing, editing); Xiaolong Chen, (Reviewing, editing); Liang Ji, (Reviewing, editing); Qiteng Hong, (Reviewing, editing).

## ACKNOWLEDGEMENTS

This work was supported by the Joint Funds of the National Natural Science Foundation of China under Grant U2166205.

## CONFLICT OF INTEREST STATEMENT

The authors declare no conflict of interest.

## DATA AVAILABILITY STATEMENT

The data that support the findings of this study are available from the corresponding author upon reasonable request.

## ORCID

*Botong Li* https://orcid.org/0000-0003-0113-3756
*Bin Li* https://orcid.org/0000-0002-7088-8274

## REFERENCES

1. Tu, J., Pan, Y., Zhang, J., Zeng, B., Jia, J., Yi, J.: Transient reactive power characteristics of HVDC during commutation failure and impact of HVDC control parameters. J. Eng. 2017(13), 1134–1139 (2017)
2. Wang, Y., Yuan, Z., Wen, W., Ji, Y., Fu, J.: Generalised protection strategy for HB-MMC-MTDC systems with RL-FCL under DC faults. IET Gener. Transm. Distrib. 12(5), 1231–1239 (2018)
3. Zhang, W., Tang, Y., Zeng, N.: Multi-terminal HVDC transmission technologies and its application prospects in China. Power Syst. Technol. 34(9), 1–6 (2010)
4. Xiang, B., Luo, J., Gao, L., Wang, J.: Protection schemes using resistive-type superconducting fault current limiters with mechanical DC circuit breakers in MMC-MTDC grids. IIET Gener. Transm. Distrib. 14(17), 3422–3432 (2020)
5. Zheng, Y., He, J., Li, B.: Research on DC protection strategy in multi-terminal hybrid HVDC system. Engineering 7, 1064–1075 (2020)
6. Liu, J., Tai, N., Fan, C.: Transient-voltage-based protection scheme for DC line faults in the multiterminal VSC-HVDC system. IEEE Trans. Power Del. 32(3), 1483–1494 (2017)
7. Li, Y., et al.: DC fault detection in MTDC systems based on transient high frequency of current. IEEE Trans. Power Del. 34(3), 950–962 (2019)
8. Li, L.X., Yao, L.: DC fault detection and location in meshed multiterminal HVDC systems based on DC reactor voltage change rate. IEEE Trans. Power Del. 32(3), 1516–1526 (2017)
9. Zhang, C., Li, Y., Song, G., Dong, X.: Fast and sensitive non-unit protection method for HVDC grids using Levenberg–Marquardt algorithm. IEEE Trans. Ind. Electron. 69(9), 9064–9074 (2022)

10. Leterme, W., Beerten, J., Hertem, D.V.: Non-unit protection of HVDC grids with inductive DC cable termination. IEEE Trans. Power Del. 31(2), 820–828 (2016)
11. Yang, J., Fletcher, J., O'Reilly, J.: Multiterminal dc wind farm collection grid internal fault analysis and protection design. IEEE Trans. Power Del. 25(4), 2308–2318 (2010)
12. Geddada, N., Yeap, Y.M., Ukil, A.: Experimental validation of fault identification in VSC-based DC grid system. IEEE Trans. Ind. Electron. 65(6), 4799–4800 (2018)
13. Han, K., Cai, Z., Xu, M.: Dynamic characteristics of characteristic parameters of traveling wave protection for HVDC transmission line and their setting. Power Syst. Technol. 27(1), 255–259 (2013)
14. Li, B., Li, Y., He, J., Li, B., Liu, S., Liu, B., Xu, L.: An improved transient traveling-wave based direction criterion for multi-terminal HVDC grid. IEEE Trans. Power Del. 35(5), 2517–2529 (2020)
15. Li, Z., Zou, G.B., Tong, B.B., Gao, H., Feng, Q.: Novel traveling wave protection method for high voltage DC transmission line. In: Proceedings of IEEE Power Energy Society General Meeting, Denver, CO, USA, pp. 1–5 (2015)
16. Zhang, C., Huang, J., Song, G., Dong, X.: Non-unit ultra-high-speed line protection for multi-terminal hybrid LCC/MMC HVDC system and its application research. IEEE Trans. Power Del. 36(5), 2825–2838 (2021)
17. Huang, Z., Liang, Y., Li, H., Wang, G.: Analytical calculation method of travelling wave for three-terminal hybrid DC system considering characteristics of T-connect bus. Autom. Electr. Power Syst. 44(17), 136–144 (2020)
18. Zhang, Y., Tai, N., Xu, B.: Fault analysis and traveling-wave protection scheme for bipolar HVDC lines. IEEE Trans. Power Del. 27(3), 1583–1591 (2012)
19. Zhang, C., Song, G., Dong, X., Huang, J.: Application research on fast line protection and adaptive restarting methods for multi-terminal hybrid LCC/MMC HVDC transmission lines. Proc. CSEE. 41(11), 3873–3884 (2021)
20. Zheng, W., Zhang, N., Yang, G.: Comparative and improvement investigation on the DC transmission line traveling wave protections of Siemens and ABB. Power Syst. Protect. Control 43(24), 149–154 (2015)

**How to cite this article:** Li, B., Li, Y., Li, B., Chen, X., Ji, L., Hong, Q.: A novel travelling-wave direction criterion for hybrid multi-terminal HVDC system. IET Gener. Transm. Distrib. 1–12 (2023). https://doi.org/10.1049/gtd2.12972